Efficient experimental identification of three-dimensional tyre structural properties

ACCEPTED MANUSCRIPT VERSION (Pre publisher typesetting)

Vasilis Tsinias [a], George Mavros [a*]

[a] Department of Aeronautical and Automotive Engineering, Loughborough University, United Kingdom

Abstract

Modal testing is routinely applied to tyres for the identification of structural parameters and prediction of their vibration response to excitations. The present work focuses on the more demanding case of modal testing with the aim of constructing a full mathematical model of a tyre, appropriate for use in a generic time-based simulation. For this purpose, the less common free-free boundary condition is employed for the wheel, while the tyre belt is excited in all three directions, namely radial tangential and lateral. To improve efficiency, a novel partial identification method is developed for the mode shapes, whereby measured and predicted frequency responses are matched around distinct resonance peaks, while eliminating the effect of out-of-band modes. Axial symmetry of the tyre requires high purity mode shapes to avoid angular dependency of the tyre's response. For this reason, experimental mode shapes are digitally filtered and combined with their orthogonal counterparts. Processed data reveals apparent repetition of selected mode shapes and this is attributed to rim deflection.

Keywords

tyre structural modelling, tyre vibration, tyre modal testing, complex mode shapes, spatial filtering

* Corresponding author

Tel: +44 (0)1509 227 237

E-mail address: g.mavros@lboro.ac.uk

List of Symbols

$A_{ij}(\omega)$	Accelerance FRF from j^{th} excitation to i^{th} measurement point
dq_r	Modal participation factor of complex mode r
$\{dx\}$	Calculated displacement vector of tyre belt
F_i	Force along the i^{th} degree of freedom
P	Number of peaks (or troughs) in a mode shape
s_r	Complex eigenvalue of r^{th} mode
$\mathbf{T_{1,2}}$	Transformation matrices from complex to real eigenvectors
$\mathbf{T_{orth}}, \mathbf{T_{tot}}$	Partial and total transformation matrices for obtaining orthogonal eigenvectors
$Y(l)$	Mode shape as a function of position along the tyre circumference
Z	Amplitude of mode shape

Greek Symbols

$\alpha_{ij}(\omega)$	Receptance FRF from j^{th} excitation to i^{th} measurement point
ξ_r	Damping ratio of r^{th} mode
φ_{ir}	i^{th} entry of the r^{th} complex eigenvector
$\mathbf{\Phi}$	Overall matrix of equivalent real eigenvectors
x_i	Measured displacement of i^{th} degree of freedom
$\mathbf{\Psi}$ or $[\Psi]$	Overall matrix of complex eigenvectors
$\{\psi_r\}$	r^{th} complex eigenvector
ω	Frequency
ω_r	Undamped natural frequency of r^{th} mode
ω_s	Spatial frequency of mode shape

1. Introduction

Modal testing of pneumatic tyres has been mainly used for identification and validation of analytical and finite element tyre models along with experimental identification of tyre properties and prediction of tyre structural response.

Z Genk et al. in [1] and A. A. Popov and Z. Genk in [2] investigated the experimental identification of tyre damping with the wheel rigidly attached to a seismic table. In these works, the general non-proportional viscous damping model is suggested as more suitable for describing tyre damping. Tyre in-plane structural properties, i.e. mode shapes, natural frequencies and damping ratios, have been identified by F. Chengjian et al. in [3] performing both single and double-input modal testing. These results reflect only the radial response of the radially excited modes. A similar – radial excitation and response – in-plane study has been carried out by D. Guan et al. in [4], in which the structural differences between radial-ply and cross-ply tyres are demonstrated for several inflation pressures. L. H. Yam et al. in [5] adopted a more complete approach as they investigated the three-dimensional tire response resulting from radial and tangential excitation forces.

The work of P. Andersson et al. in [6] investigates the influence of different tread patterns on the modal properties of the tyre while research conducted by I. Lopez et al. in [7] and [8] examines the effect of rotation on the dynamic response of the tyre and consequently on the observed eigenvalues. Typically, experimentally identified modal quantities may be used for the validation or parameterisation of a FE (Finite Element) model. For example, the response of a FE model is compared to modal data in the work of Y. Guan et al. in [9]. The reconstruction of a mathematical model of the tyre represents the ultimate use of modal information. F. Chengjian and G. Dihua in [10] and D. Guan et al. in [11] have developed vertical and enveloping models using modal parameters in an analytical context.

The present work presents a new method for efficient testing and post-processing for identification of high purity in-plane and out-of-plane tyre modal parameters. In this context, high

purity refers to free-from-noise mode shapes. A decision has been made to focus on the free-free boundary condition whereby the wheel is suspended from elastic chords. This is done with a view of using the identified modal parameters for the reconstruction of a generic mathematical model of a tyre's structure that can be paired with a model of a suspension in a full-vehicle multi-body dynamics simulation [12]. The work herein focuses on the identification of the modal data and does not include the construction of the final tyre structural model. A passenger car tyre is used for demonstration of the method with its modal parameters identified and presented in the paper.

2. Theoretical background

For a tyre structure represented by N nodes and 3N degrees of freedom (radial, tangential and lateral per node), the relationship between the excitation and deformation vectors is expressed as follows:

$$\begin{bmatrix} x_1(\omega) \\ x_2(\omega) \\ \vdots \\ x_{3N}(\omega) \end{bmatrix} = \begin{bmatrix} \alpha_{11}(\omega) & & \alpha_{13N}(\omega) \\ \alpha_{21}(\omega) & & \alpha_{23N}(\omega) \\ \vdots & \cdots & \vdots \\ \alpha_{3N1}(\omega) & & \alpha_{3N3N}(\omega) \end{bmatrix} \cdot \begin{bmatrix} F_1(\omega) \\ F_2(\omega) \\ \vdots \\ F_{3N}(\omega) \end{bmatrix} \quad (1)$$

where x_i is the deformation of the i^{th} degree of freedom, F_j is the force applied on the j^{th} degree of freedom and α_{ij} is the respective receptance FRF (Frequency Response Function). As each node is defined in the three-dimensional space, the elements of the two vectors included in eq. (1) are presented in nodal groups consisting of three elements each:

$$\begin{bmatrix} \begin{Bmatrix} {}_{r}X_1 \\ {}_{l}X_1 \\ {}_{t}X_1 \end{Bmatrix} \\ \begin{Bmatrix} {}_{r}X_2 \\ {}_{l}X_2 \\ {}_{t}X_2 \end{Bmatrix} \\ \vdots \\ \begin{Bmatrix} {}_{r}X_N \\ {}_{t}X_N \\ {}_{l}X_N \end{Bmatrix} \end{bmatrix} = \begin{bmatrix} \alpha_{11}(\omega) & & \alpha_{13N}(\omega) \\ \alpha_{21}(\omega) & & \alpha_{23N}(\omega) \\ \vdots & \cdots & \vdots \\ \alpha_{3N1}(\omega) & & \alpha_{3N3N}(\omega) \end{bmatrix} \cdot \begin{bmatrix} \begin{Bmatrix} {}_{r}F_1 \\ {}_{l}F_1 \\ {}_{t}F_1 \end{Bmatrix} \\ \begin{Bmatrix} {}_{r}F_2 \\ {}_{l}F_2 \\ {}_{t}F_2 \end{Bmatrix} \\ \vdots \\ \begin{Bmatrix} {}_{r}F_N \\ {}_{t}F_N \\ {}_{l}F_N \end{Bmatrix} \end{bmatrix} \quad (2)$$

The deformation of each node is defined with respect to a local, nodal-specific radial/tangential/lateral frame of reference, as shown in figure 1.

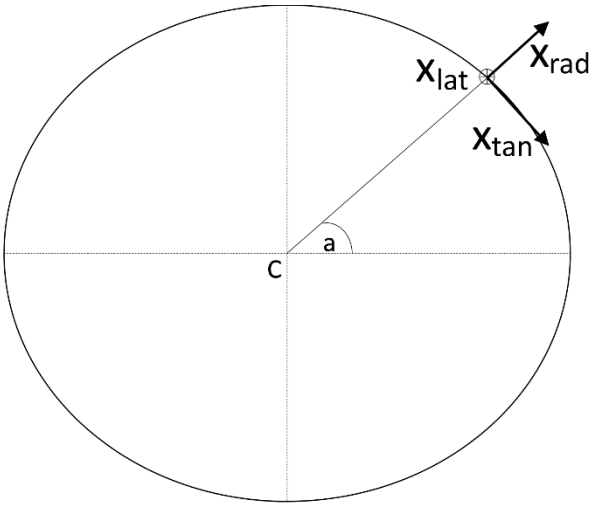

Figure 1 – Nodal coordinate system

The coordinate system shown in figure 1 indicates the axes along which acceleration is measured during testing. The radial direction is defined by axis X_{rad} which is normal to the surface of the tyre and points outward of the surface. Axis X_{tan} defines the tangential direction which is orthogonal to X_{rad} and points clockwise. The lateral axis X_{lat} is obtained as the cross product of X_{rad} and X_{tan} and points into the page. As shown on the left-hand-side of eq. (2), the deformation triplets measured in the nodal frame of reference are arranged in the following order: radial, lateral and tangential for all the measurement nodes. From eq. (2) it is evident that $(3N)^2$ frequency

response functions are required to fully describe a tyre. Such a large number may impose a significant challenge in terms of modal testing. To minimise the necessary number of frequency response functions, the principle of reciprocity is applied according to which:

$$\alpha_{ij}(\omega) = \alpha_{ji}(\omega) \tag{3}$$

This assumption is shown to be valid in [1], [2]. Due to eq. (3), only the upper or the lower triangular matrix of the FRF matrix in eq. (2) needs to be experimentally identified. Moreover, due to the non-proportional nature of tyre belt damping, the elements of the FRF matrix are expressed as follows [13]:

$$\alpha_{ij}(\omega) = \sum_{r=1}^{m} \left[\frac{\varphi_{ir}\varphi_{jr}}{a_r(i\omega - s_r)} + \frac{(\varphi_{ir}\varphi_{jr})^*}{a_r^*(i\omega - s_r^*)} \right] \tag{4}$$

where $\varphi_{ir}\varphi_{jr}$ is the residue of mode r, a_r is the scaling factor of mode r set equal to unity, $()^*$ denotes the complex conjugate of the quantity in the brackets and s_r is the r^{th} eigenvalue of the tyre belt:

$$s_r = -\omega_r\xi_r + i\omega_r\sqrt{1-\xi_r^2} \tag{5}$$

In eq. (5), ω_r is the undamped natural frequency and ξ_r is the damping ratio of mode r. The numerators of the fractions in eq. (4) form the eigenvector matrix, comprising the first m tyre belt eigenvectors:

$$[\Psi] = \begin{bmatrix} \varphi_{11} & \varphi_{12} & & \varphi_{1(m-1)} & \varphi_{1m} \\ \vdots & \vdots & \ddots & \vdots & \vdots \\ \varphi_{3N1} & \varphi_{3N2} & & \varphi_{3N(m-1)} & \varphi_{3Nm} \end{bmatrix}_{3Nxm} = [\{\psi_1\} \quad \dots \quad \{\psi_m\}] \tag{6}$$

Equations (2), (4) and (6) reveal that, due to consistency of modal constants [14], the tyre belt structure can be described by obtaining only three consecutive rows or columns corresponding to a particular node:

$$\begin{bmatrix} \begin{Bmatrix} {}_{r}X_1 \\ {}_{l}X_1 \\ {}_{t}X_1 \end{Bmatrix} \\ \begin{Bmatrix} {}_{r}X_2 \\ {}_{l}X_2 \\ {}_{t}X_2 \end{Bmatrix} \\ \vdots \\ \begin{Bmatrix} {}_{r}X_N \\ {}_{t}X_N \\ {}_{l}X_N \end{Bmatrix} \end{bmatrix} = \begin{bmatrix} \alpha_{1,3(j-1)+1} & \alpha_{1,3(j-1)+2} & \alpha_{1,3(j-1)+3} \\ \alpha_{2,3(j-1)+1} & \alpha_{2,3(j-1)+2} & \alpha_{2,3(j-1)+3} \\ \alpha_{3,3(j-1)+1} & \alpha_{3,3(j-1)+2} & \alpha_{3,3(j-1)+3} \\ \alpha_{4,3(j-1)+1} & \alpha_{4,3(j-1)+2} & \alpha_{4,3(j-1)+3} \\ \alpha_{5,3(j-1)+1} & \alpha_{5,3(j-1)+2} & \alpha_{5,3(j-1)+3} \\ \alpha_{6,3(j-1)+1} & \alpha_{6,3(j-1)+2} & \alpha_{6,3(j-1)+3} \\ \vdots & \vdots & \vdots \\ \alpha_{3N-2,3(j-1)+1} & \alpha_{3N-2,3(j-1)+2} & \alpha_{3N-2,3(j-1)+3} \\ \alpha_{3N-1,3(j-1)+1} & \alpha_{3N-1,3(j-1)+2} & \alpha_{3N-1,3(j-1)+3} \\ \alpha_{3N,3(j-1)+1} & \alpha_{3N,3(j-1)+2} & \alpha_{3N,3(j-1)+3} \end{bmatrix}_{3Nx3} \cdot \begin{Bmatrix} {}_{r}F_j \\ {}_{l}F_j \\ {}_{t}F_j \end{Bmatrix} \quad (7)$$

By comparing eq. (7) and eq. (1), it becomes clear that the number of the required FRF has been reduced from the initial $(3N)^2$ to a more manageable number of 9N. This approach not only allows for a more economical and efficient modal testing procedure; it does so without any loss of fundamental information [12]. At this point, to enhance experimental efficiency with minimal loss of accuracy, an ad hoc assumption is made that *there is no exchange of energy between in and out-of-plane modes* [12]. According to this assumption an in-plane excitation will not trigger an out-of-plane mode and vice versa. This simplification does not apply in practice but can be considered harmless. Firstly, it was found that the lateral response to radial excitation was insignificant and difficult to confirm as a genuine lateral response to radial excitation, or conversely to dismiss as a lateral response due to small misalignment of the excitation probe and/or other similar effects. Essentially, it is difficult to robustly identify the cross-talk between radial/tangential and lateral directions, as the level of the response lies generally within the experimental noise band. Secondly, it must be emphasised that the measured mode-shapes are

true in their respective directions and for as long as they refer to the tread centre-line and small, linear deflections. A tyre model based on the identified mode shapes would provide realistic belt deflection at small lateral slip but no associated change in tyre radius because of that slip. This is a tolerable limitation of such a model. Of course, at very large (non-linear) slip, the radius of the tyre would be expected to change slightly because of that slip. This would involve highly non-linear material/geometry interactions that are clearly not captured by a linear decoupled modal model. The sated simplification significantly reduces the workload imposed by modal testing, as it further reduces the required FRFs from 9N to 5N. This reduction is reflected in the following expression:

$$\begin{bmatrix} \begin{Bmatrix} {}_{r}X_1 \\ {}_{l}X_1 \\ {}_{t}X_1 \end{Bmatrix} \\ \begin{Bmatrix} {}_{r}X_2 \\ {}_{l}X_2 \\ {}_{t}X_2 \end{Bmatrix} \\ \vdots \\ \begin{Bmatrix} {}_{r}X_N \\ {}_{t}X_N \\ {}_{l}X_N \end{Bmatrix} \end{bmatrix} = \begin{bmatrix} \alpha_{1,3(j-1)+1} & 0 & \alpha_{1,3(j-1)+3} \\ 0 & \alpha_{2,3(j-1)+2} & 0 \\ \alpha_{3,3(j-1)+1} & 0 & \alpha_{3,3(j-1)+3} \\ \alpha_{4,3(j-1)+1} & 0 & \alpha_{4,3(j-1)+3} \\ 0 & \alpha_{5,3(j-1)+2} & 0 \\ \alpha_{6,3(j-1)+1} & 0 & \alpha_{6,3(j-1)+3} \\ \vdots & \vdots & \vdots \\ \alpha_{3N-2,3(j-1)+1} & 0 & \alpha_{3N-2,3(j-1)+3} \\ 0 & \alpha_{3N-1,3(j-1)+2} & 0 \\ \alpha_{3N,3(j-1)+1} & 0 & \alpha_{3N,3(j-1)+3} \end{bmatrix}_{3Nx3} \cdot \begin{Bmatrix} {}_{r}F_j \\ {}_{l}F_j \\ {}_{t}F_j \end{Bmatrix} \quad (8)$$

Having derived the structure of the receptance matrix, the next step is to experimentally identify the quantities populating the FRF matrix of eq. (8).

3. Experimental layout

The experimental parameters and the equipment used to populate eq. (8) are presented in table 1:

Table 1

Experimental parameters & equipment (for full details see [12])

Tyre	Continental 195/50 R15
Sampling rate	20000 [Hz]
Analogue band-pass filter	[1 3000] [Hz]
Force transducer	Brüel & Kjær – Type 8230
Accelerometer	Brüel & Kjær – Type 4332

Charge Amplifier	Brüel & Kjær – Nexus Type 2691-A-0S2
Modal Shaker	Brüel & Kjær – LDS V201
Acquisition Card	NI PCIe-6259

Similar works conducted in the past propose two different approaches regarding the boundary condition of the tyre. In the work of Z. Geng et al. in [1] the tyre is attached to a seismic table. In contrast, the free-free boundary condition is adopted by L. H. Yam et al. in [15]. In this paper the latter approach is followed with the tyre vertically suspended by several elastic bands ensuring that the excitation force of each test is applied along a direction normal to the direction defined by the primary axis of each band so as to minimise any reaction forces, see figures 2 and 3 and ref. [12].

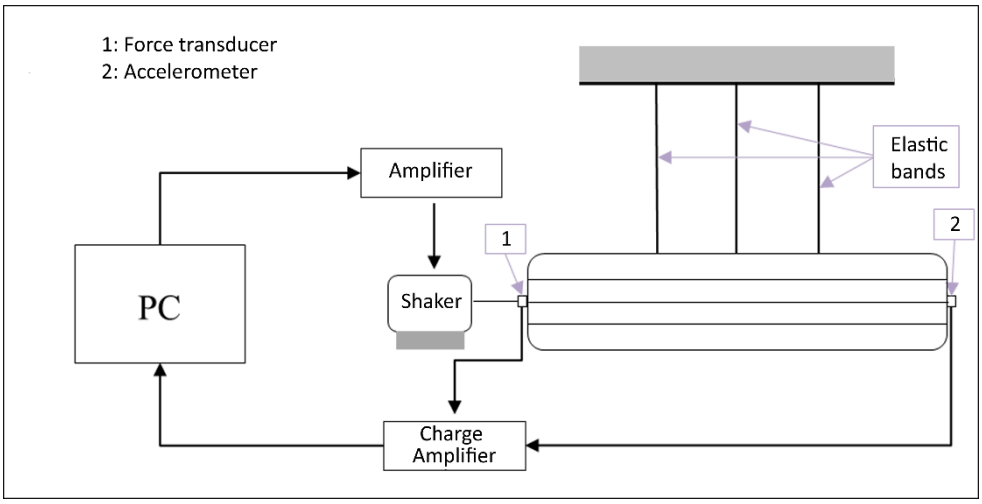

Figure 2 – Experimental layout (in-plane excitation)

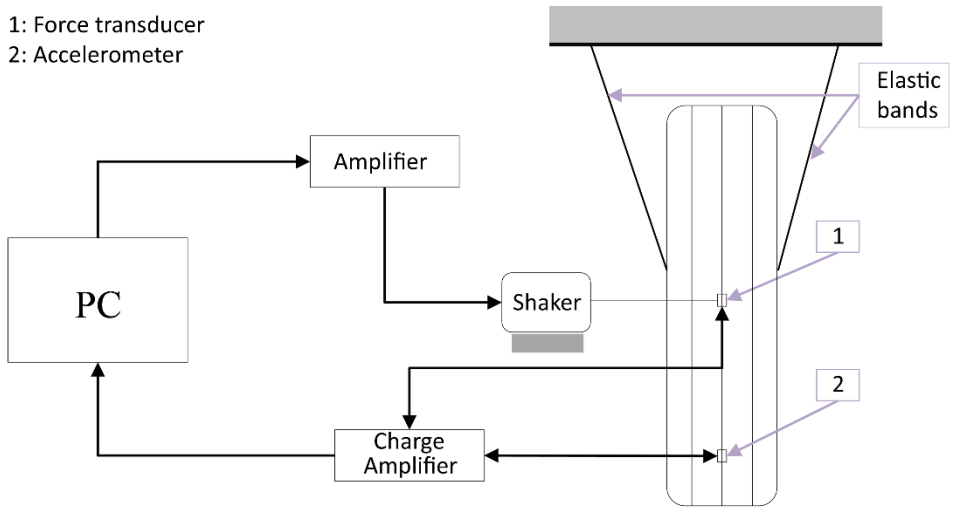

Figure 3 – Experimental layout (out-of-plane excitation)

Adoption of the free-free boundary condition aligns with the scope of the proposed modal testing procedure, which is the identification of tyre modal properties to be implemented in a simulation environment. To fully understand the necessity of having the tyre freely suspended, one may consider the origin of the eigenproperties of any mechanical system, i.e. the solution of the eigenproblem formulated by the system of homogeneous differential equations of motion. By rigidly fixing in space any point of the structure, the respective columns and rows of the abovementioned system are omitted and consequently the eigenproperties obtained by the new eigenproblem are not related exclusively to the structure under investigation, but they depend on the adopted attachment method as well. Further, if a structure is to be accelerated in space by a generic load vector, the modal description of this structure must correspond to one that includes the rigid body modes. These rigid modes need not be identified themselves as they are easy to derive from the structure's mass and geometry; however, the identified flexible modes should belong to the set that contains the rigid modes as well.

The tyre is represented by 30 equi-spaced nodes along its circumference. As implied by eq. (8), the excitation force is applied on a single node. Several possible excitation methods are proposed by D. J. Ewins in [13]. In the present work, white Gaussian noise is preferred to a periodic excitation. The downside of using a periodic excitation, for example a sinusoidal frequency sweep,

is the deterministic relation between the excitation at the moment of examination and the excitation applied at every previous moment. In that case, a deterministic relation will exist in the response history of the structure as well, and this relation will influence the identified properties. To overcome this problem, the frequency components of the excitation signal must be defined in a stochastic rather than a deterministic manner, hence the use of a Gaussian excitation.

The excitation force and the respective acceleration of every belt node are expressed in the frequency domain and thus the accelerance function is calculated. To populate the FRF matrix of eq. (8), the experimentally obtained accelerance functions are transformed into receptance functions as follows:

$$\alpha_{ij}(\omega) = -\frac{A_{ij}(\omega)}{\omega^2} \tag{9}$$

where $\alpha_{ij}(\omega)$ is the receptance function corresponding to the i^{th} and the j^{th} node and $A_{ij}(\omega)$ is the respective accelerance function.

4. Post processing and identified properties

4.1 Initial post processing

Having experimentally populated the receptance FRF matrix of eq. (8), the next step is the estimation of the modal properties of interest, namely the residue and the eigenvalue of each mode. Keeping in mind the non-proportional nature of tyre damping and combining eq. (4) and (5), the following expression for the receptance functions holds:

$$\alpha_{ij}(\omega) = \sum_{r=1}^{m}\left[\frac{\varphi_{ir}\varphi_{jr}}{\left(\omega_r\xi_r + i\left(\omega - \omega_r\sqrt{1-\xi_r^2}\right)\right)} + \frac{\varphi_{ir}^*\varphi_{jr}^*}{\left(\omega_r\xi_r + i\left(\omega + \omega_r\sqrt{1-\xi_r^2}\right)\right)}\right] \tag{10}$$

Index m approaches infinity as new modes are included at increasing frequency. In practice though, there is an upper identifiable value of m which mainly depends on the experimental layout and the equipment used. This implies that there will always exist out of band residual modes, which are expressed by terms C_1 and C_3:

$$\alpha_{ij}(\omega) = \overbrace{-\frac{1}{\omega^2 M_{ij}^R}}^{C_1} + \overbrace{\sum_{r=1}^{m}\left[\frac{\varphi_{ir}\varphi_{jr}}{\left(\omega_r\xi_r + i\left(\omega - \omega_r\sqrt{1-\xi_r^2}\right)\right)} + \frac{\varphi_{ir}^*\varphi_{jr}^*}{\left(\omega_r\xi_r + i\left(\omega + \omega_r\sqrt{1-\xi_r^2}\right)\right)}\right]}^{C_2} + \overbrace{\frac{1}{K_{ij}^R}}^{C_3} \tag{11}$$

These residual terms are included within the experimentally obtained frequency response functions. As a result, the modal quantities of eq. (10) cannot be directly identified and an indirect approach is required instead. Initially, the area surrounding each resonance of any particular FRF – where a single mode is dominant – is examined separately, see figure 4. This area requires a minimum of one term of eq. (4) describing the overall FRF. In practice additional terms may be included to improve accuracy in the neighbourhood of the resonance. In the current work, the sum of two terms has been used as shown in eq. (12).

$$\alpha_{ij}^{\omega_1\to\omega_2}(s) = \frac{A_1}{s - s_1} + \frac{(A_1)^*}{s - (s_1)^*} + \frac{A_2}{s - s_2} + \frac{(A_2)^*}{s - (s_2)^*} \tag{12}$$

The eigenvalue which yields a natural frequency closer to the resonance frequency is the most accurate estimate for that particular mode.

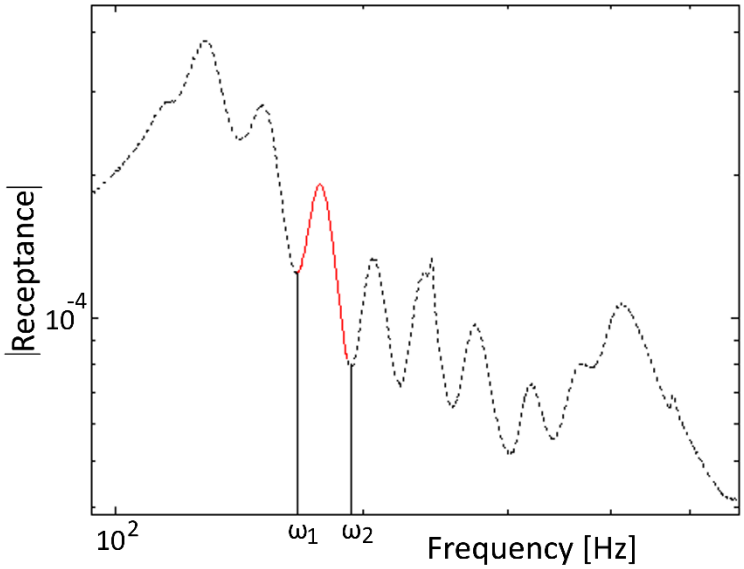

Figure 4 – Identification of an FRF in the neighbourhood of a single resonance

On the contrary, the respective residue cannot be obtained via the numerators in eq. (12), as the residual terms C_1 and C_3 of eq. (11) are also included in the measured response but not accounted for in eq. (12). Hence an alternative approach must be adopted. B. J. Dobson in [16] proposed an identification method which considers the out-of-band modes and the resulting identified properties refer only to the modes of interest. This was achieved by assuming that the residual terms C_1 and C_3 are constant near each resonance. Dobson's method was developed for cases with hysteretic damping, so an alternative version to allow for the identification of structures with non-proportional damping is proposed here. The starting point for the new method is the equation describing the receptance FRF of the r^{th} mode, as follows:

$$ {}_r\alpha_{ij}(\omega) = \frac{\varphi_{ir}\varphi_{jr}}{(i\omega - s_r)} + \frac{\varphi_{ir}^{*}\varphi_{jr}^{*}}{(i\omega - s_r^{*})} + K \Rightarrow $$

$$ {}_r\alpha_{ij}(\omega) = \frac{{}_rA_{ij} + {}_rB_{ij}i}{(i\omega - s_r)} + \frac{\left({}_rA_{ij} - {}_rB_{ij}i\right)}{(i\omega - s_r^{*})} + K \Rightarrow $$

$$ {}_r\alpha_{ij}(\omega) = \frac{\left({}_rA_{ij} + {}_rB_{ij}i\right)(i\omega - s_r^*) + \left({}_rA_{ij} - {}_rB_{ij}i\right)(i\omega - s_r)}{(i\omega - s_r)(i\omega - s_r^*)} + K \tag{13} $$

where K stands for the effect of the remaining modes on ${}_r\alpha_{ij}(\omega)$. If ω_f is a frequency close to the natural frequency of mode r, the respective value of the FRF is:

$$ {}_r\alpha_{ij}(\omega_f) = \frac{\left({}_rA_{ij} + {}_rB_{ij}i\right)(i\omega_f - s_r^*) + \left({}_rA_{ij} - {}_rB_{ij}i\right)(i\omega_f - s_r)}{(i\omega_f - s_r)(i\omega_f - s_r^*)} + K \tag{14} $$

As mentioned above, it is assumed that the residual term K remains constant in the vicinity of mode r and can be eliminated by defining a new function [12]:

$$ D(\omega) = \left({}_r\alpha_{ij}(\omega) - {}_r\alpha_{ij}(\omega_f)\right)(i\omega - s_r)(i\omega - s_r^*)(i\omega_f - s_r)(i\omega_f - s_r^*) \tag{15} $$

The main property of the above relation is that the residual term K is eliminated by subtraction in the first set of brackets (term ${}_r\alpha_{ij}(\omega) - {}_r\alpha_{ij}(\omega_f)$), which allows for the identification of the pure residue of mode r. Substitution of eq. (13) and (14) into eq. (15) yields the following quadratic expression:

$$ D(\omega) = \left(2\,{}_rA_{ij}\omega_f i - 2\,{}_rA_{ij}a - 2\,{}_rB_{ij}b\right)\omega^2 + \left(-2\,{}_rA_{ij}\omega_f^2 i - 2(a^2 + b^2)i + 2\left(-2\,{}_rA_{ij}a - 2\,{}_rB_{ij}b\right)ai\right)\omega + C \tag{16} $$

where a and b represent the real and the imaginary parts of the eigenvalue s_r respectively.

Having identified the r^{th} eigenvalue of the system using eq. (12) and having experimentally obtained the receptance FRF close to the respective resonance, it is possible to express eq. (15) as follows:

$$D(\omega) = K_1\omega^2 + K_2\omega + K_3 \tag{17}$$

By comparing the analytical terms of eq. (16) with the associated experimentally identified terms of eq. (17), the real and imaginary parts of the residue are estimated as follows:

$$\left.\begin{aligned} \Lambda_1 = \mathrm{Re}(K_1) = -2\ {}_rA_{ij}a - 2\ {}_rB_{ij}b \\ \Lambda_2 = \mathrm{Im}(K_1) = 2\ {}_rA_{ij}\omega_f \end{aligned}\right\} \Rightarrow$$

$$\begin{aligned} {}_rA_{ij} &= \frac{\Lambda_2}{2\omega_f} \\ {}_rB_{ij} &= \frac{-2\ {}_rA_{ij}a - \Lambda_1}{2b} \end{aligned} \tag{18}$$

The only required parameter in the above procedure is the fixing frequency ω_f which, if selected close to the natural frequency of mode r, should not affect the estimated values of ${}_rA_{ij}$ and ${}_rB_{ij}$. Nevertheless, due to experimentally induced errors in calculating $\Lambda 1$ and $\Lambda 2$ and numerical inaccuracy in estimating the eigenvalue of mode r, terms ${}_rA_{ij}$ and ${}_rB_{ij}$ are found to vary slightly for different fixing frequencies, resulting in different FRF curves, as depicted in figure 5.

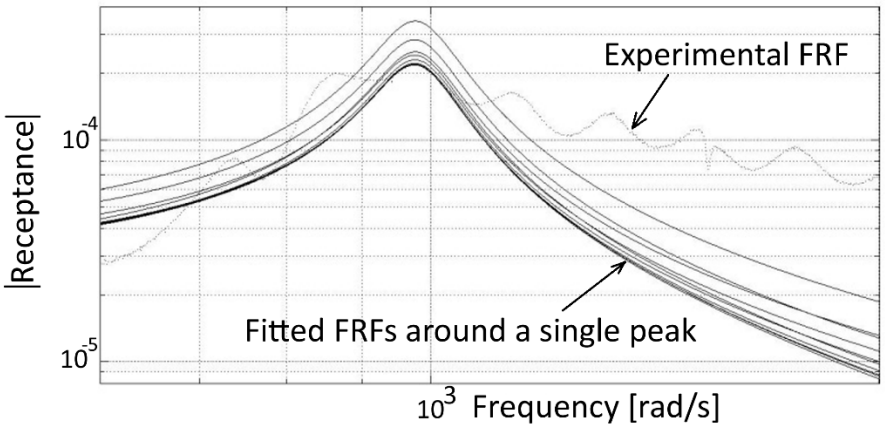

Figure 5 – Variations of the fitted FRF with fixing frequency ω_f

Considering that mode r is dominant around the resonant frequency ω_r, the most accurate amongst the curves presented in the above figure is the one which minimises the selection criterion of expression (19):

$$\left|\left|\alpha(\omega_r)_{exp}\right| - \left|\ {}_r\alpha(\omega_r)_{est}\right|\right| \to 0 \qquad (19)$$

By applying this criterion, the optimum pair of ${}_rA_{ij}$ and ${}_rB_{ij}$ is obtained:

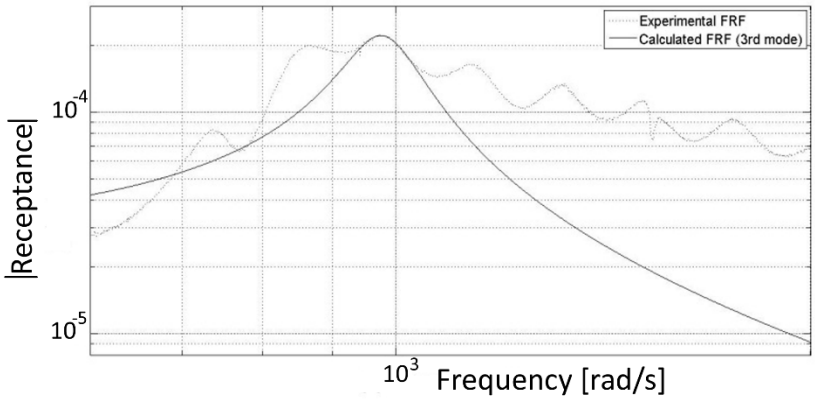

Figure 6 – Final fitting around a single peak of the FRF

The application of the above procedure on the response functions acquired along the circumference of the tyre leads to the calculation of the associated eigenvectors. Having obtained the residues of every radially excited mode, the respective residue vector is formulated:

$$\begin{aligned}&\{{}_{\mathrm{rad}}\mathrm{A}+{}_{\mathrm{rad}}\mathrm{Bi}\}\\&=[\varphi_1\varphi_1\quad 0\quad \varphi_3\varphi_1\quad \cdots\quad \varphi_{\mathrm{k}}\varphi_1\quad 0\quad \varphi_{(\mathrm{k}+2)}\varphi_1\quad \cdots\quad \varphi_{(3\mathrm{N}-2)}\varphi_1\quad 0\quad \varphi_{3\mathrm{N}}\varphi_1]^{\mathrm{T}}\end{aligned}\tag{20}$$

The complex eigenvector associated with the above residue vector is obtained by:

$$\{\psi_{\mathrm{r}}\}=\frac{\{{}_{\mathrm{r}}\mathrm{A}+{}_{\mathrm{r}}\mathrm{Bi}\}}{\varphi_1}\Rightarrow$$

$$\{\psi_{\mathrm{r}}\}=[\varphi_1\quad 0\quad \varphi_3\quad \ldots\quad \varphi_{3\mathrm{N}-3}\quad 0\quad \varphi_{3\mathrm{N}}]^{\mathrm{T}}\tag{21}$$

Similarly, for the tangentially excited modes:

$$\begin{aligned}&\{{}_{\tan}\mathrm{A}+{}_{\tan}\mathrm{Bi}\}\\&=[\varphi_1\varphi_3\quad 0\quad \varphi_3\varphi_3\quad \cdots\quad \varphi_{\mathrm{k}}\varphi_3\quad 0\quad \varphi_{(\mathrm{k}+2)}\varphi_3\quad \cdots\quad \varphi_{(3\mathrm{N}-2)}\varphi_3\quad 0\quad \varphi_{3\mathrm{N}}\varphi_3]^{\mathrm{T}}\end{aligned}\tag{22}$$

$$\{\psi_{\mathrm{t}}\}=\frac{\{{}_{\tan}\mathrm{A}+{}_{\tan}\mathrm{Bi}\}}{\varphi_3}\Rightarrow$$

$$\{\psi_{\mathrm{t}}\}=[\varphi_1\quad 0\quad \varphi_3\quad \ldots\quad \varphi_{3\mathrm{N}-3}\quad 0\quad \varphi_{3\mathrm{N}}]^{\mathrm{T}}\tag{23}$$

and for the laterally excited modes:

$$\{{}_{\mathrm{lat}}\mathrm{A}+{}_{\mathrm{lat}}\mathrm{Bi}\}=[0\quad \varphi_2\varphi_2\quad 0\quad \ldots\quad 0\quad \varphi_{\mathrm{k}}\varphi_2\quad 0\quad \ldots\quad 0\quad \varphi_{(3\mathrm{N}-1)}\varphi_2\quad 0]^{\mathrm{T}}\tag{24}$$

$$\{\psi_{\mathrm{l}}\}=\frac{\{{}_{\mathrm{lat}}\mathrm{A}+{}_{\mathrm{lat}}\mathrm{Bi}\}}{\varphi_2}\Rightarrow$$

$$\{\psi_l\} = [0 \quad \varphi_2 \quad 0 \quad ... \quad 0 \quad \varphi_{3N-1} \quad 0]^T \tag{25}$$

4.2 Identified properties

The fitting procedure described by eq. (12) is applied to the in-plane and the out-of-plane modes of the tyre, providing the respective natural frequencies and damping ratios. Table 2 presents these quantities for the case of in-plane radially excited modes, table 3 for the in-plane tangentially excited modes and table 4 for the out-of-plane laterally excited modes.

Table 2

In-plane Radial Modes (after [12])

Mode	Nat. Freq. [Hz] (radial resp.)	Nat Freq. [Hz] (tangential resp.)	Delta [%]	Damp. Ratio [%] (radial resp.)	Damp. Ratio [%] (tangential resp.)
1	115	118	2.58	3.63	3.81
2	131	133	1.51	6.19	5.91
3	155	153	1.30	6.61	6.28
4	180	180	0.00	5.93	6.26
5	208	207	0.48	5.48	6.05
6	242	241	0.41	3.28	2.35
7	275	276	0.36	5.81	5.91
8	320	321	0.31	5.61	6.71
9	371	370	0.27	6.87	6.87
10	413	420	1.68	7.05	5.77

Table 3

In-plane Tangential Modes (after [12])

Mode	Nat. Freq. [Hz] (radial resp.)	Nat Freq. [Hz] (tangential resp.)	Delta [%]	Damp. Ratio [%] (radial resp.)	Damp. Ratio [%] (tangential resp.)

1	108	106	1.87	4.14	3.54
2	116	117	0.86	4.22	4.09
3	134	135	0.74	6.50	6.63
4	153	150	1.98	6.06	6.25
5	177	177	0.00	5.28	6.48
6	196	198	1.02	4.23	8.18
7	207	208	0.48	4.64	5.26
8	236	238	0.84	4.47	4.24
9	273	272	0.37	4.51	4.56
10	318	318	0.00	4.74	4.58
11	375	375	0.00	5.95	5.18
12	404	403	0.25	4.06	4.59
13	473	459	3.00	1.64	2.20

Table 4

Out-of-plane Modes (after [12])

Mode	Natural Frequency [Hz]	Damping Ratio [%]
1	59.39	2.75
2	72.95	4.83
3	103.19	4.38
4	114.91	3.70
5	131.26	4.49
6	152.63	5.50
7	174.56	4.78
8	195.14	4.38
9	216.03	3.44
10	246.21	3.67
11	274.12	4.68

As expected, for the cases where the response of each node is measured along the radial and the tangential directions, there is agreement in terms of natural frequency (see [5]). This agreement is quantified by the Delta function:

$$\text{Delta} = \frac{|\omega_r - \omega_t|}{(\omega_r + \omega_t)/2} \tag{26}$$

It is evident that in both cases of in-plane modes the natural frequency discrepancy along different response directions is kept below 3%.

Table 4 suggests the existence of two out-of-plane modes (59.39 and 72.95 Hz) which do not correspond to any in-plane mode. These modes represent the translational out-of-phase/out-of-plane motion of the belt with respect to the rim. In these low-frequency lateral modes the belt displaces with respect to the rim without flexing, hence there is no coupling with tangential or radial modes. This relative displacement is shown later when the relevant mode shapes are plotted.

The identified eigenvectors are complex, which indicates of non-standing waves. This complexity, which derives from the non-proportional nature of tyre damping, is evident in the Argand diagrams in figures 7-11 where the eigenvector components are distributed in the phase range [-180^o 180^o].

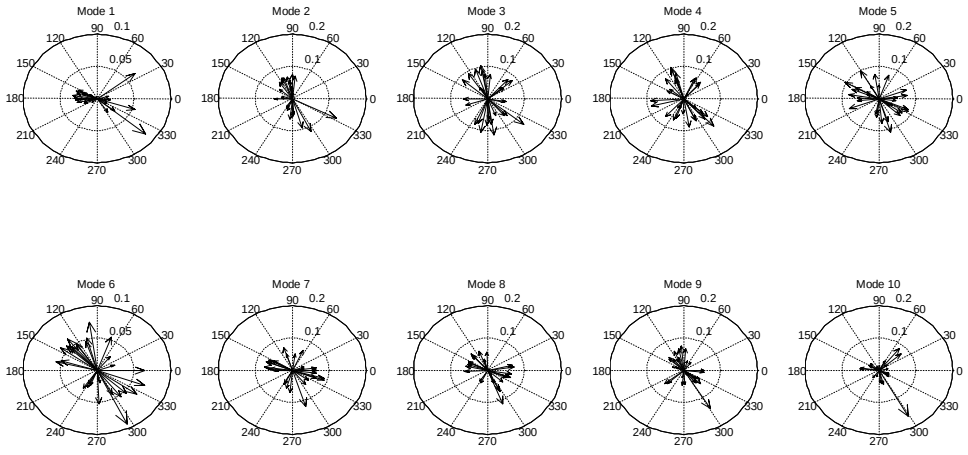

Figure 7 – Argand diagrams: complex radial modes, radial response

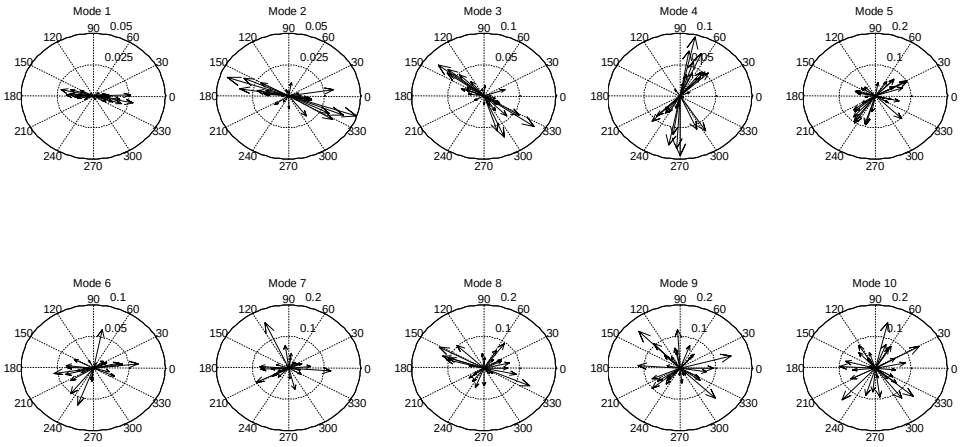

Figure 8 – Argand diagrams: complex radial modes, tangential response

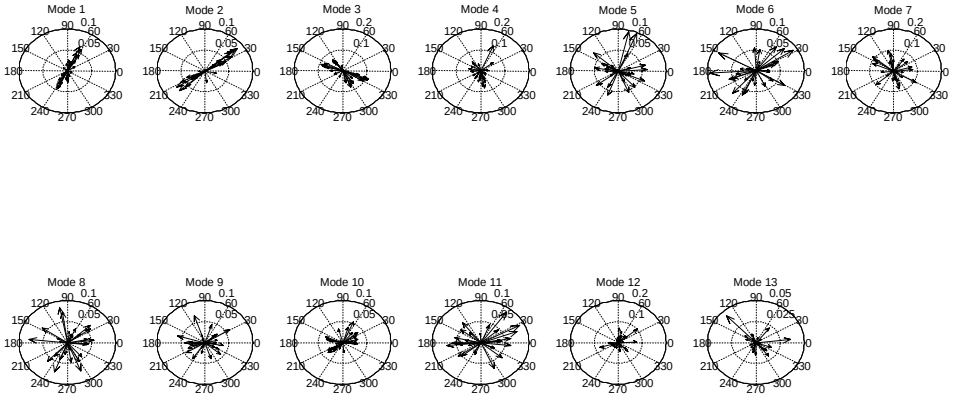

Figure 9 – Argand diagrams: complex tangential modes, radial response

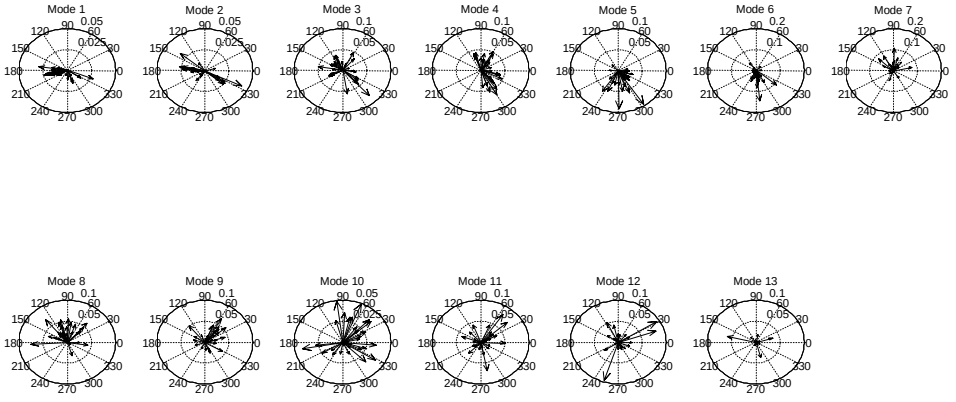

Figure 10 – Argand diagrams: complex tangential modes, tangential response

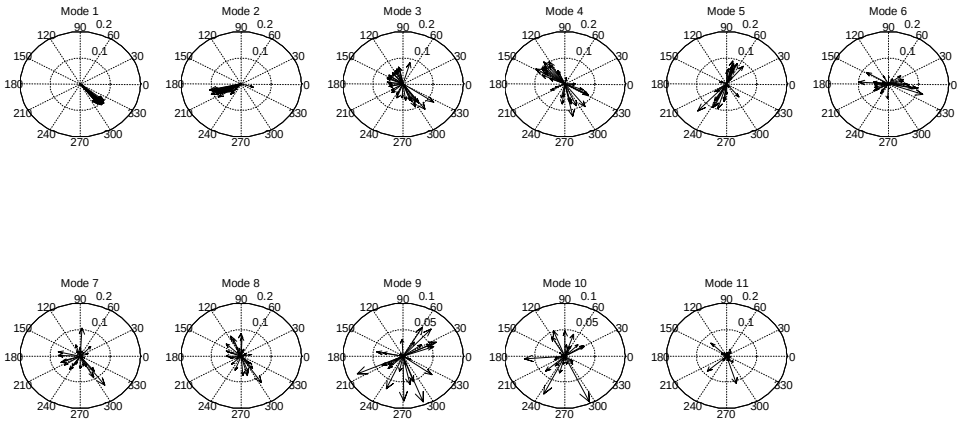

Figure 11 – Argand diagrams: complex lateral modes, lateral response

4.3 Complex to real normal modes

Although the experimentally identified complex modes presented in the previous section may be used in a simulation environment – which is the broader scope of the present research – the equivalent real modes need to be calculated for validation purposes and for comparison with previously published results. Amongst several transformation methods, the one developed by N. Niedbal in [17] is implemented in the present work. According to this approach, the real and the complex eigenvectors are related via the following transformation:

$$\mathbf{\Phi} = \mathbf{\Psi T_1 T_2} \tag{27}$$

where $\mathbf{\Phi}$ and $\mathbf{\Psi}$ are the real and complex eigenvector matrices respectively and $\mathbf{T_1}$, $\mathbf{T_2}$ are transformation matrices. The first step is the calculation of transformation matrix $\mathbf{T_1}$, the real part of which is set equal to the identity matrix and the imaginary part is obtained by the following expression:

$$\mathrm{Im}(\mathbf{T_1}) = -\left(\mathrm{Re}\left(\mathbf{\Psi^T}\right)\mathrm{Re}(\mathbf{\Psi})\right)^{-1}\mathrm{Re}\left(\mathbf{\Psi^T}\right)\mathrm{Im}(\mathbf{\Psi})\mathrm{Re}(\mathbf{T_1}) \tag{28}$$

Having calculated the transformation matrix $\mathbf{T_1}$ and having experimentally identified the eigenvalues of the system, the following two auxiliary matrices are obtained [12]:

$$\mathbf{M} = \mathbf{T_1^T T_1} \tag{29}$$

$$\mathbf{K} = \mathbf{T_1^T}[\mathbf{s^2}]\mathbf{T_1} \tag{30}$$

The eigenproblem formulated by the above two matrices yields the second transformation matrix $\mathbf{T_2}$:

$$[\mathbf{K} - [f_r^2]\mathbf{M}]\ \mathbf{T_2} = \{0\} \tag{31}$$

The real eigenvectors of the system are obtained by substitution of transformation matrices $\mathbf{T_1}$ and $\mathbf{T_2}$ in eq. (27). These real eigenvectors lead to the real radial, tangential and lateral mode shapes shown in figures 12-16 (also see [12] for full detail).

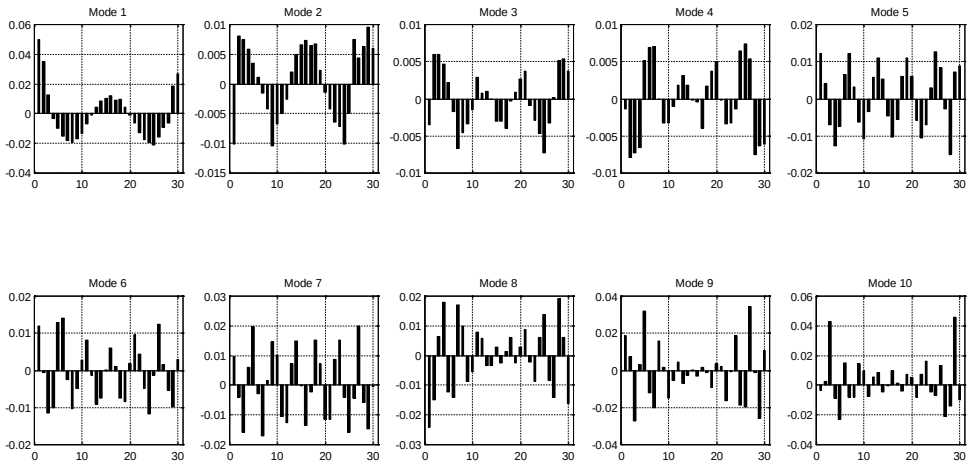

Figure 12 – Real mode shapes obtained via radial response to radial excitation

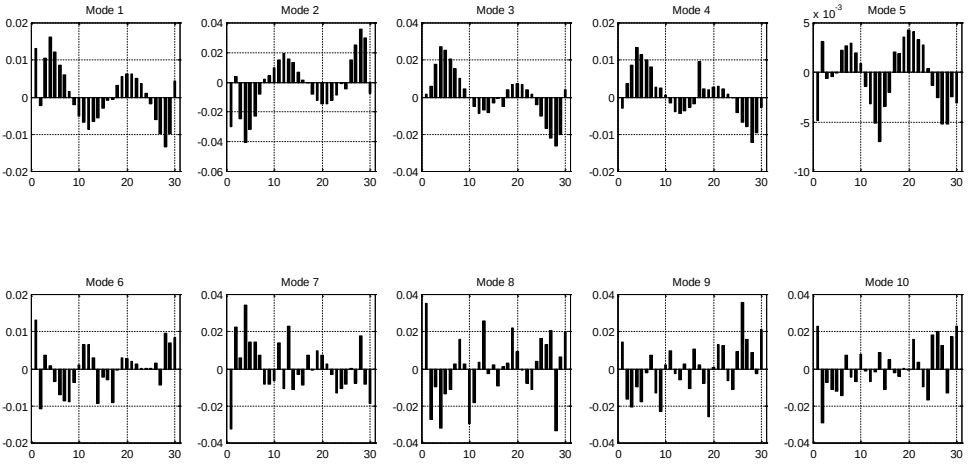

Figure 13 – Real mode shapes obtained via tangential response to radial excitation

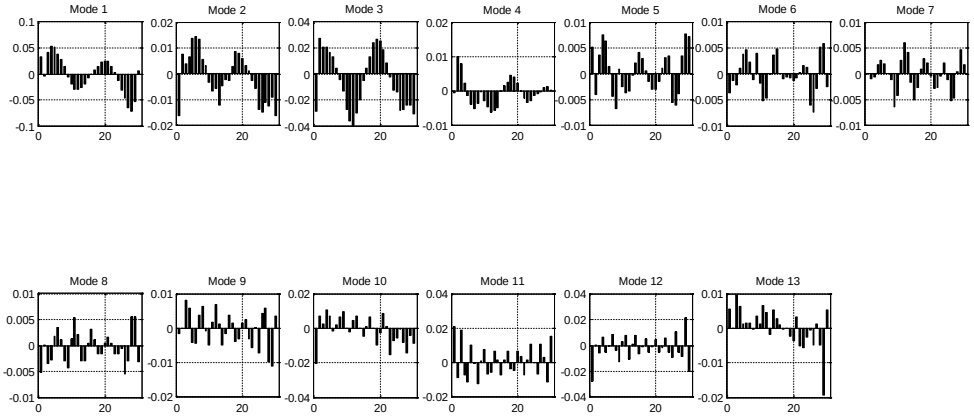

Figure 14 – Real mode shapes obtained via radial response to tangential excitation

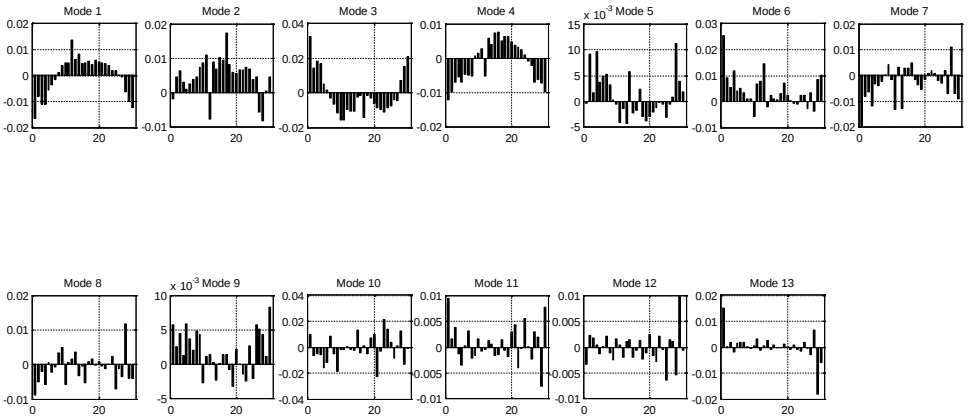

Figure 15 – Real mode shapes obtained via tangential response to tangential excitation

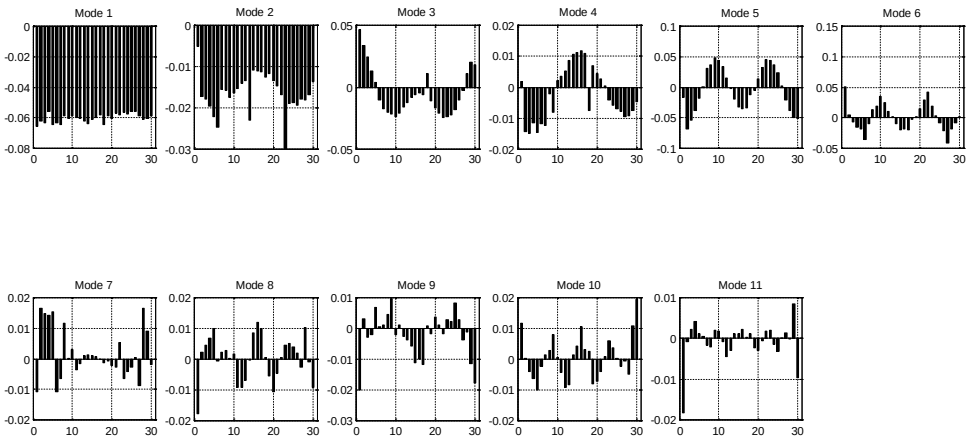

Figure 16 – Real mode shapes obtained via lateral response to lateral excitation

4.4 Digital filtering of mode shapes

Real tyre belt mode shapes have been previously obtained analytically [18] and it is proposed that each mode shape is a sinusoid of amplitude Z and of a single spatial frequency (ω_s), along the circumference of the tyre belt (variable l):

$$Y(l) = Z\sin(\omega_s l) \tag{32}$$

Visual inspection of the real mode shapes calculated in the previous section (figures 12-16) shows the presence of significant noise in the expected sinusoids. To quantify the amount of noise, the identified mode shapes are transformed in the spatial frequency domain using the Fast Fourier Transform. As an example, figure 17 shows the spatial frequency content of the 2nd radial mode of the tyre.

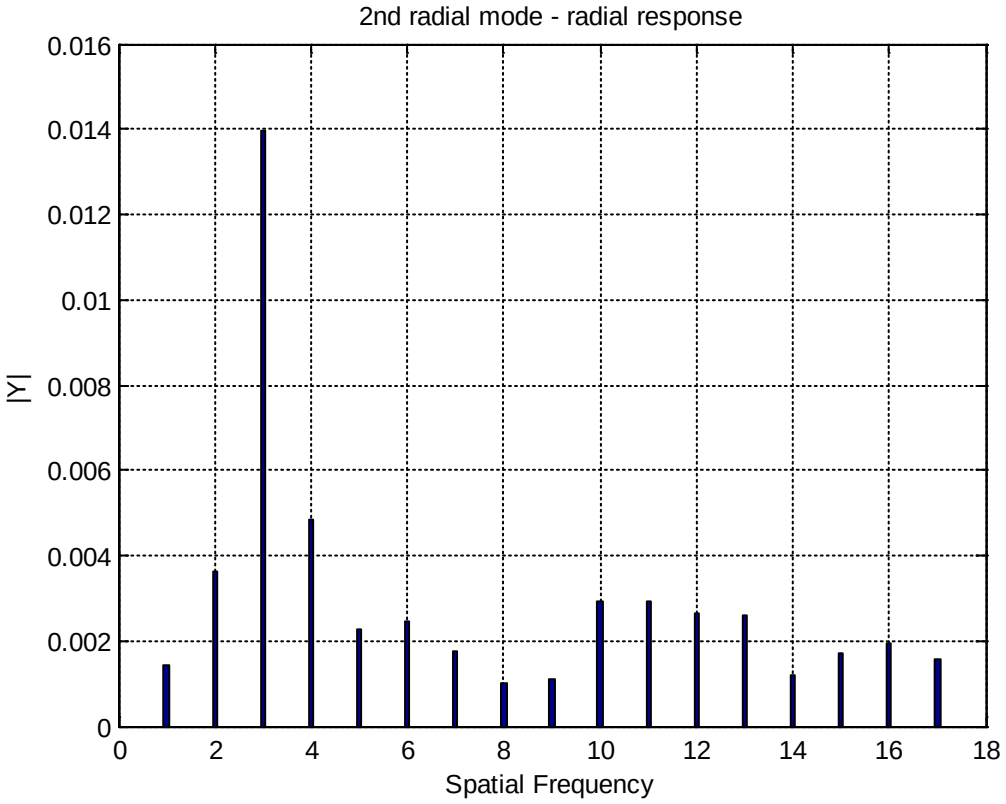

Figure 17 – Spatial frequency spectrum

From figure 17 it is evident that there is one dominant spatial frequency component (r_{max}) and this is true for every identified mode shape. To eliminate noise, filtering is applied according to eq. (33) and the new spatial frequency spectrum – figure 18 – consists of a single sinusoidal form, see eq. (34).

$$Z_i \sin(\omega_{si} l) = 0 \; for \; all \; i \neq r_{max} \tag{33}$$

$$Y(l) = Z_{r_{max}} \sin\left(\omega_{sr_{max}} l\right) \tag{34}$$

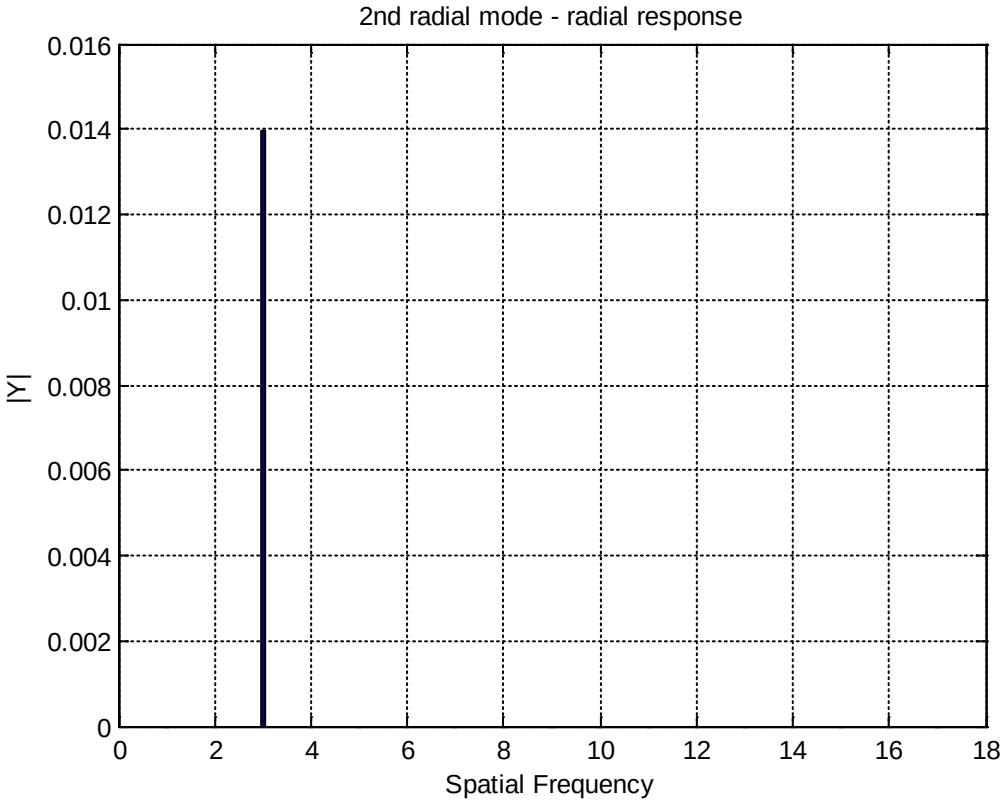

Figure 18 – Spatial frequency spectrum (digitally filtered)

Thus, without any loss of fundamental information (since the dominant spatial frequency is retained in whole), this digital filtering procedure allows for noise-free mode shapes which – when coupled with the phase of the original complex modes – can be readily implemented in a tyre simulation environment. The resulting filtered real mode-shapes for all modes are shown in figures 19-28, see also ref. [12].

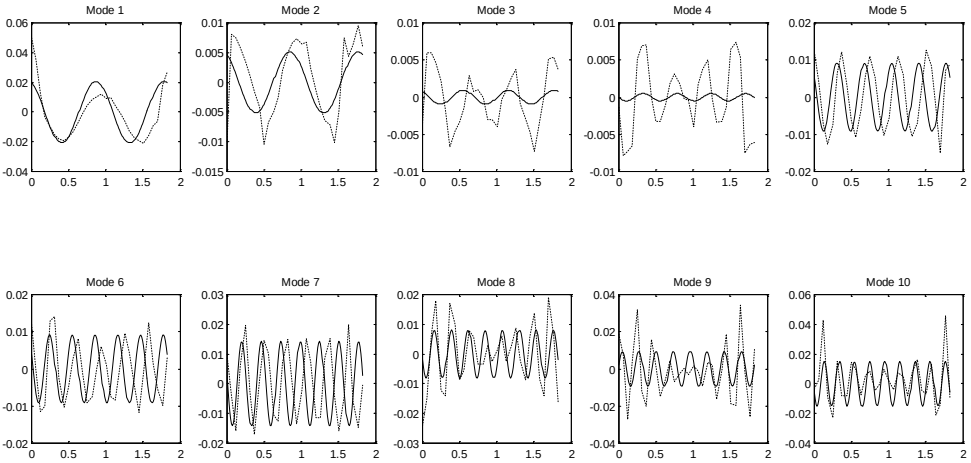

Figure 19 – Radial response to radial excitation: comparison of original (dotted lines) and filtered (solid lines) mode shapes

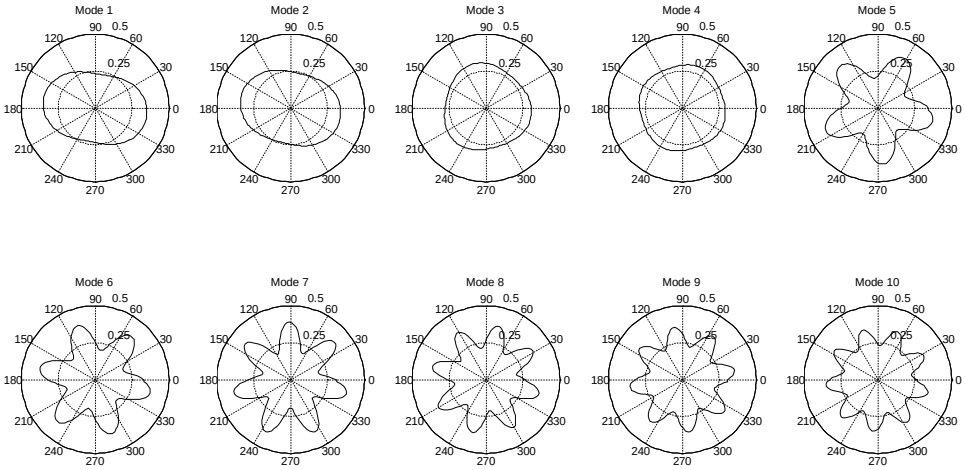

Figure 20 – Polar plots of modes obtained from radial response to radial excitation

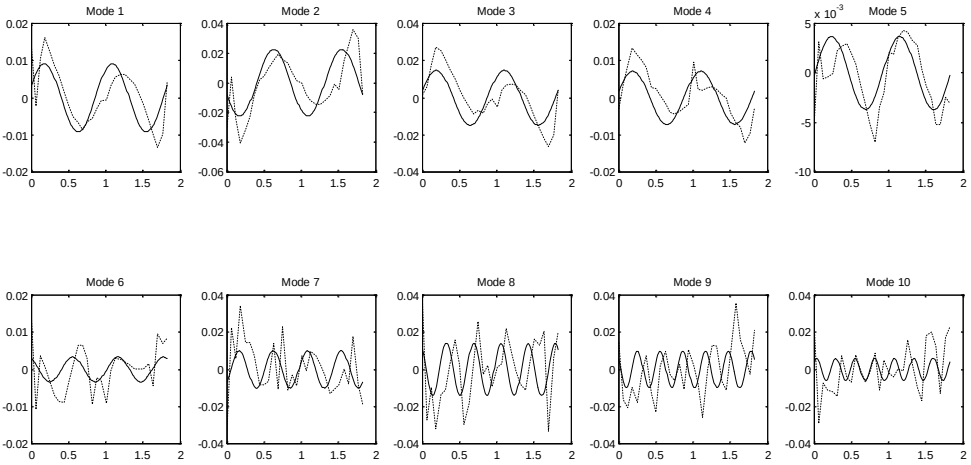

Figure 21 – Tangential response to radial excitation: comparison of original (dotted lines) and filtered (solid lines) mode shapes

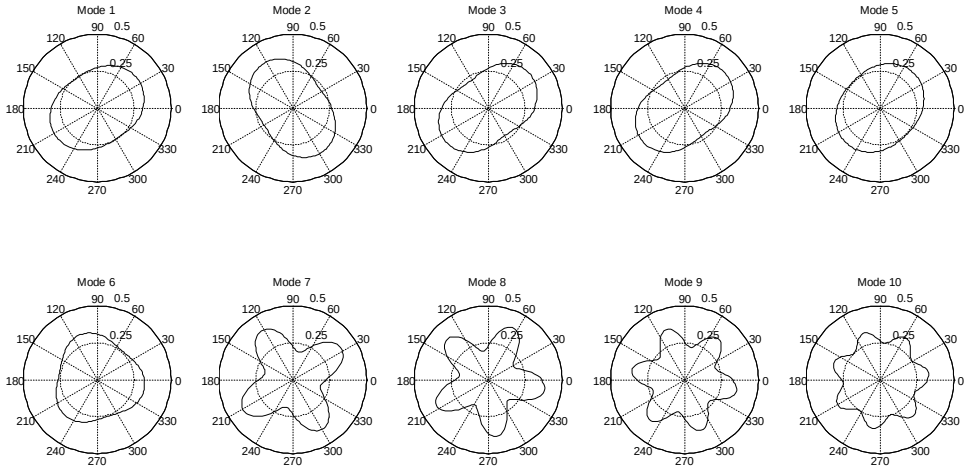

Figure 22 – Polar plots of modes obtained from tangential response to radial excitation

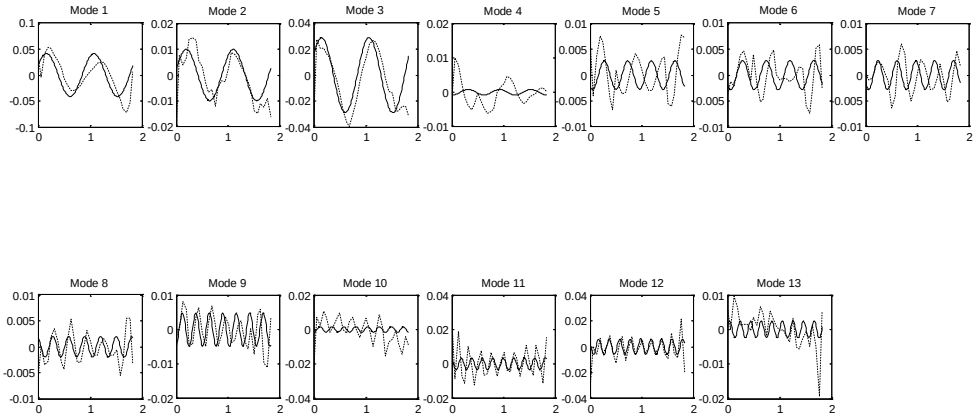

Figure 23 – Radial response to tangential excitation: comparison of original (dotted lines) and filtered (solid lines) mode shapes

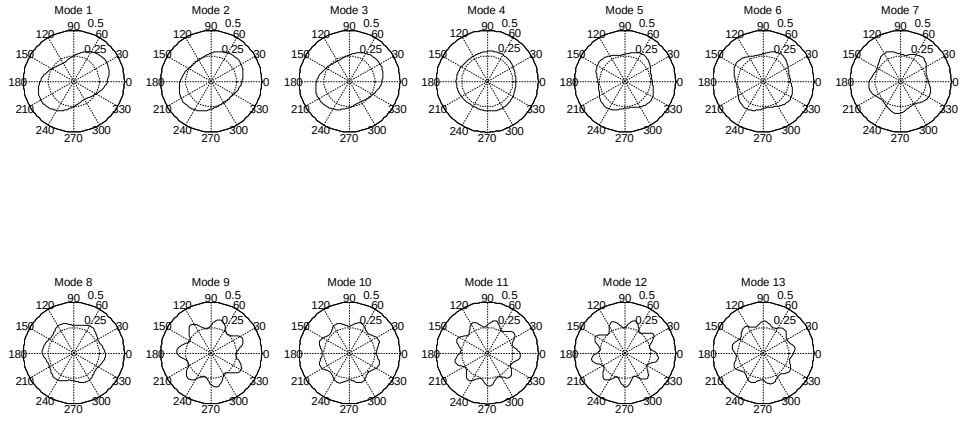

Figure 24 – Polar plots of modes obtained from radial response to tangential excitation

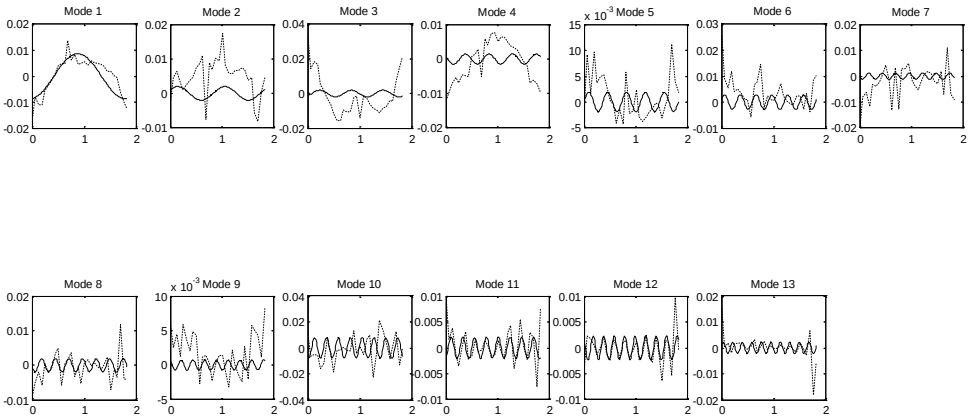

Figure 25 – Tangential response to tangential excitation: comparison of original (dotted lines) and filtered (solid lines) mode shapes

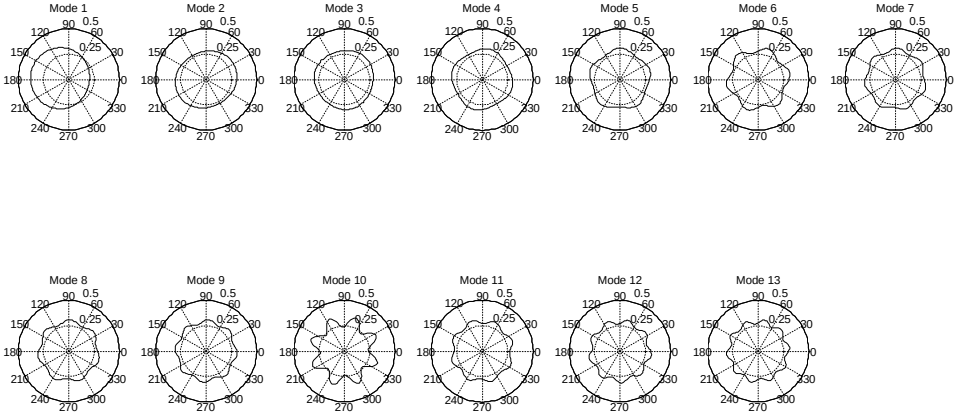

Figure 26 – Polar plots of modes obtained from tangential response to tangential excitation

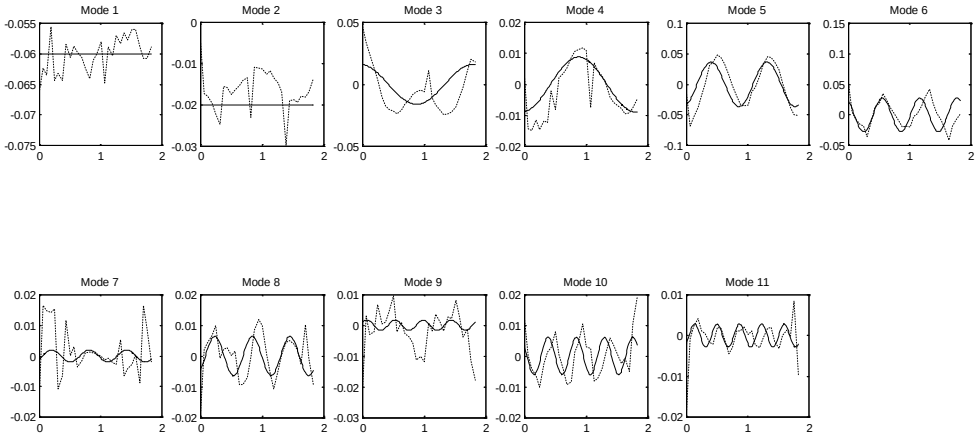

Figure 27 – Lateral response to lateral excitation: comparison of original (dotted lines) and filtered (solid lines) mode shapes

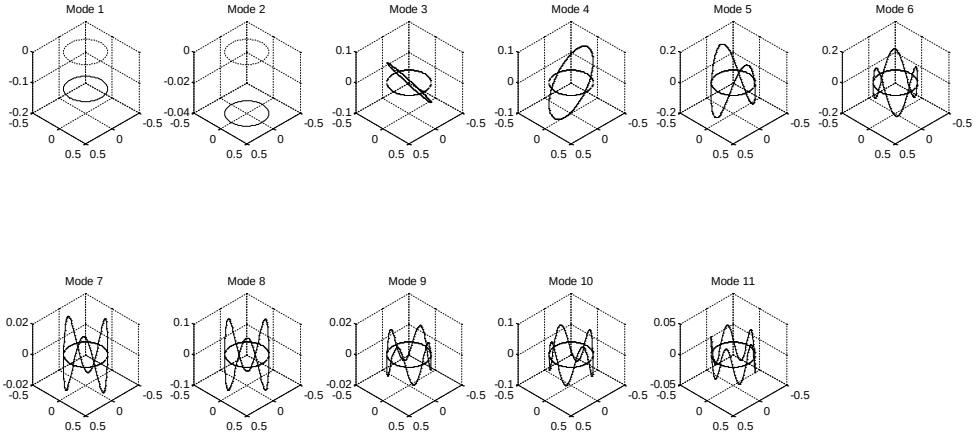

Figure 28 – Three-dimensional real lateral mode shapes

The frequencies associated with the first two lateral modes in figure 28 (59.39 Hz and 72.95 Hz, see also table 4) do not correspond to any in-plane modes and this is because these modes do not include lateral flexing of the belt as mentioned earlier.

4.5 Apparent repetition of mode shapes

The modes presented in the above section include several occasions of repeated mode shapes, which are not found in previous analytical and experimental results, since a particular pattern of tyre belt deformation cannot occur in more than one natural frequencies. To further study these spurious modes, the motion of the rim was measured and examined. Tables 5 and 6 summarise the state of the tyre belt and the rim for each problematic mode. The asterisk (*) indicates modes which include combined rim and belt resonances. Analysis of the rim motion revealed that for any set of repeated mode shapes there is only one mode featuring pure belt deformation. The remaining modes describe a different state of tyre-rim motion, as belt deformation is coupled with flexing of the rim. In the current work these rim deflections are omitted under the assumption of a rigid rim and only the flexible belt modes are considered.

Table 5

Repeated radial mode shapes

116.5 Hz (*)	132.0 Hz
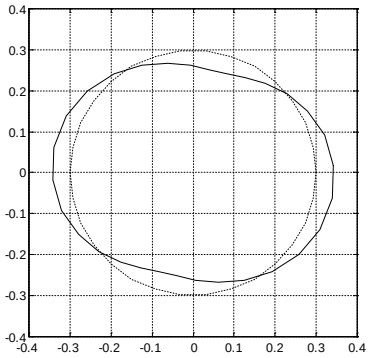	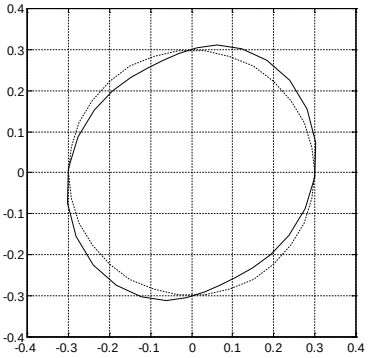

Table 6

Repeated lateral mode shapes

59.4 Hz (*)	73.0 Hz (*)
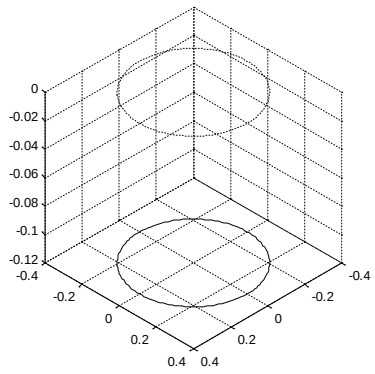	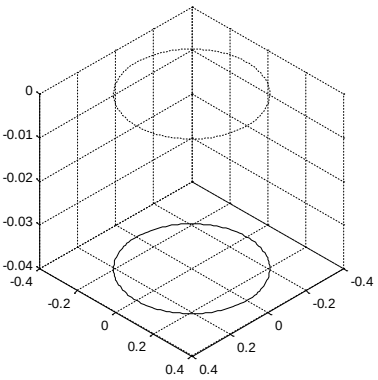
103.2 Hz (*)	**114.9 Hz (*)**
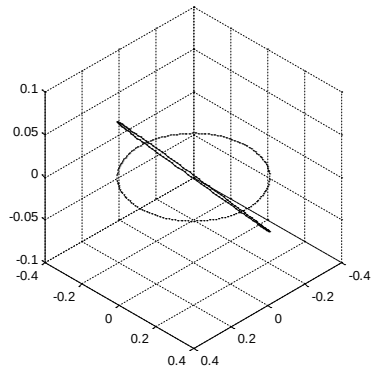	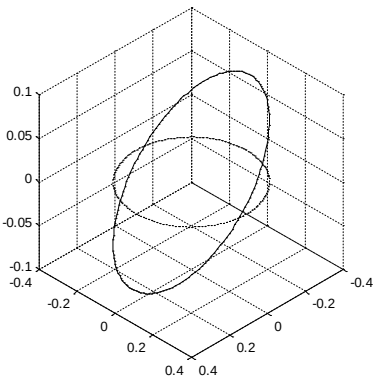

152.6 Hz (*)	174.6 Hz (*)	195.1 Hz
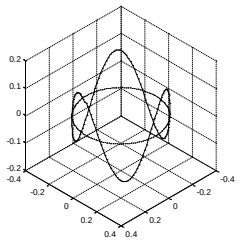	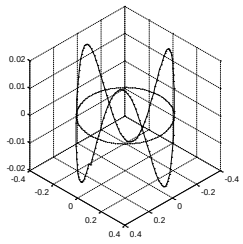	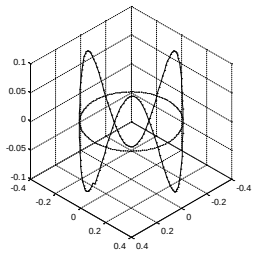

216.0 Hz	246.2 Hz (*)
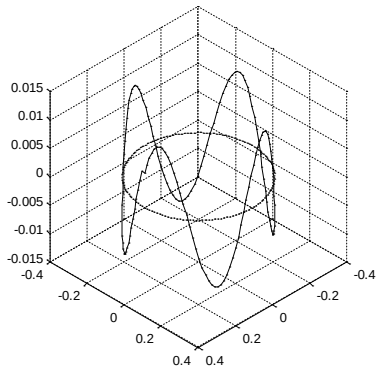	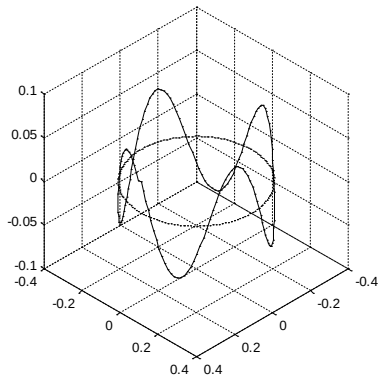

4.6 Orthogonal modes

Because of symmetry in tyre geometry [13], the identified set of mode shapes is not generally sufficient to predict belt deformation under any arbitrary excitation. Dealing with arbitrary deformations is necessary when the identified modal model is to be used as a tyre model in multi-body simulation [12]. To overcome this limitation, an orthogonal mode set is required so that the deformation of the belt is obtained as a linear combination of the deformation (participation factor) of each mode and its orthogonal counterpart. To illustrate this, the spatial deformation of the belt due to a single mode is considered as follows:

$$\{dx\} = dq_r\{\psi_r\} \tag{35}$$

Where $\{\psi_r\}$ is the eigenvector of mode r, dq_r is the corresponding modal participation factor and $\{dx\}$ is the deformation vector of the structure.

The eigenvector $\{\psi_r\}_{orth}$ which is orthogonal to $\{\psi_r\}$ is obtained by rotating this initial eigenvector by an angle $\delta\varphi$. The value of $\delta\varphi$ depends on each mode shape and specifically the number of peaks contained within it and is given by the following equation:

$$\delta\varphi = {}^{\pi}/_{p} \tag{36}$$

where p is the number of peaks (or troughs) contained within the initial mode shape. Looking at the first identified radial mode as an example, p=2 and the rotation angle is $\delta\varphi=45^{o}$. This angle is used in the calculation of the transformation matrix of each node as follows:

$$\mathbf{T_{orth}} = \begin{bmatrix} \cos(\delta\varphi) & 0 & -\sin(\delta\varphi) \\ 0 & 1 & 0 \\ \sin(\delta\varphi) & 0 & \cos(\delta\varphi) \end{bmatrix} \tag{37}$$

and the calculation of the overall transformation matrix:

$$\mathbf{T_{tot}} = \begin{bmatrix} \mathbf{T_{orth}} & \cdots & 0 \\ \vdots & \ddots & \vdots \\ 0 & \cdots & \mathbf{T_{orth}} \end{bmatrix} \tag{38}$$

Having obtained the overal transformation matrix, the new orthogonal eigenvector derives from the following equation:

$$\{\psi_r\}_{orth} = \mathbf{T_{tot}}\{\psi_r\} \tag{39}$$

Equation (40) represents an alternative version of eq. (35), which has been extended to include the initial (term A) and the associated orthogonal eigenvector (term B) of the first radial mode:

$$\{dx\} = \overbrace{dq_1\{\psi_1\}}^{A} + \overbrace{dq_1^{orth}\{\psi_1\}_{orth}}^{B} \quad (40)$$

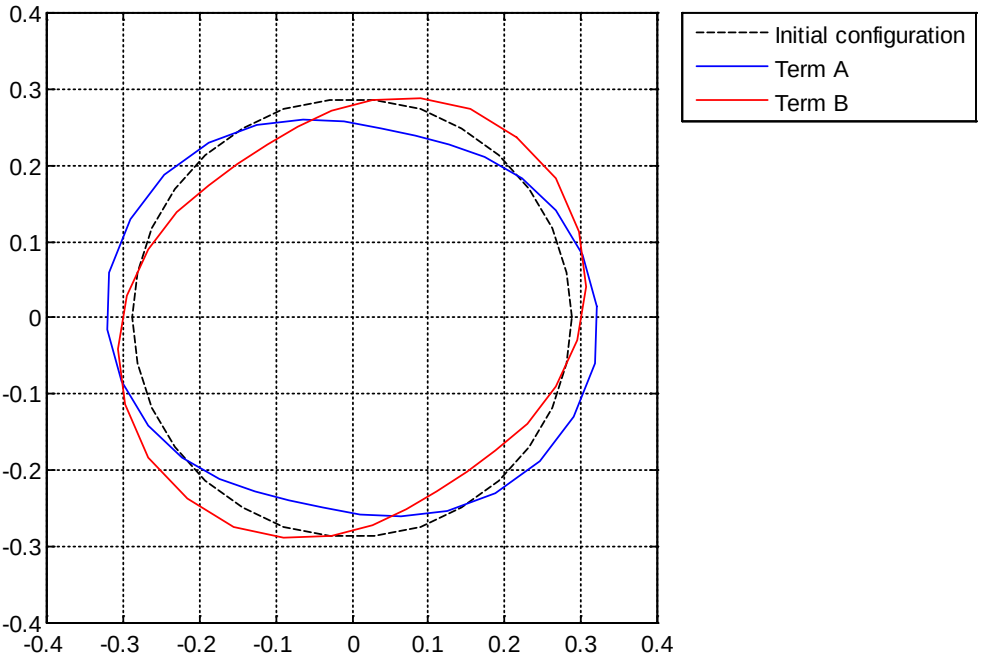

Figure 29 – 1st radial mode and its orthogonal

The first radial mode and its associated orthogonal mode obtained using eq. (39) are shown in figure 29. Application of this procedure to every experimentally identified mode yields the following expression for the calculation of the total deformation vector:

$$\{dx\} = \sum_{r=1}^{m} dq_r\{\psi_r\} + \sum_{r=1}^{m} dq_r^{orth}\{\psi_r\}_{orth} \quad (41)$$

where m is the total number of identified modes. This approach allows for describing any possible belt deformation up to the maximum natural frequency of the modes included in eq. (41).

5. Conclusions

The structural parameters of a pneumatic tyre have been experimentally identified. The tyre was suspended freely in space, with the excitation force during each test being perpendicular to the supporting elastic bands to minimise reaction forces. The tyre belt was excited along the radial, tangential and lateral direction of the first node using a white noise signal. The in-plane response of every node was acquired for the radially and the tangentially excited modes. For the case of lateral modes, the lateral response of each node was obtained.

Excitation and response signals were processed in the frequency domain, providing the elements of the FRF matrix which were used to estimate eigenvalues by application of a typical rational fraction polynomial method. The natural frequency and the damping ratio of each mode are calculated directly from these experimentally identified eigenvalues. Good agreement is found between natural frequencies obtained for the same mode along different response directions. Moreover, there is good correlation between the natural frequencies of radial, tangential, and lateral modes although the out-of-plane modes include two additional modes to the in-plane ones. In both these additional out-of-plane modes, the tyre belt moves laterally with respect to the rim without flexing, hence there is no coupling with in-plane modes.

The identification of the residue of each mode presented a challenge, as the neighbourhood of the experimentally obtained frequency response function around the resonance of a specific mode is influenced by all the remaining modes. Considering the non-proportionality of tyre belt damping, a new identification method was developed which eliminates these residual terms allowing for the exclusive identification of the mode residue under investigation. This identification process allowed calculation of the complex eigenvector matrix. The complex eigenvectors were transformed into real ones for inspection and comparison with similar published results. To enhance the quality of the obtained data, all spatial eigenvectors were transformed into the spatial frequency domain and the dominant spatial frequency of each mode shape was identified. The remaining frequency components were eliminated and the mode shapes were reconstructed using only the dominant spatial frequency. Visual inspection of the digitally filtered waveforms revealed several repeated mode shapes, an observation which does not agree with the literature, or expectation. To investigate further, the motion of the rim was acquired and processed. This

showed that for every case of repeated mode shapes there is one mode of exclusive belt resonance, at most. In the remaining repeated modes, the belt resonance is coupled with rim resonance so these modes describe a different state of the tyre/rim assembly. Moreover, to fully describe any possible configuration of the belt – up to the maximum experimentally identified natural frequency – a second set of modes was analytically calculated. This set of mode derives by rotation of the original modes, to create orthogonal pairs.

The final step is the reverse transformation from real to complex modes. This is achieved by coupling the digitally filtered real modes with the complex phase component of the experimentally identified complex modes.

The main sources of error in the suggested procedure are the narrow-bandwidth partial identification of residues by assumption of a constant contribution of out-of-band modes, as well as digital filtering of the eigenvectors in the spatial domain. The latter point requires further explanation. With the suggested filtering, the underlying dominant sinusoid is maintained, while all spatial noise is removed from the eigenvector. This is appropriate if a perfectly symmetric tyre is required. However, if the aim is to model a specific real tyre with potential manufacturing asymmetries, it is possible that some of the rejected noise is due to inherent asymmetric behaviour of the tyre. The current procedure does not distinguish between genuine asymmetries and experimentally induced noise, resulting always in perfectly symmetric eigenvectors. Inherent asymmetries could manifest as additional vibration and harshness during tyre operation in a full vehicle simulation environment. Clearly, this information would be missing from the model. Despite this shortcoming, preliminary attempts to synthesize a tyre model from modal data obtained by the suggested method have been largely successful, with the synthesized tyre model showing very good correlation with the real tyre in terms of vertical stiffness, while also capturing the expected increase of relaxation length with vertical load [12], [19].

Although the developed procedure is thorough enough to allow synthesizing a tyre model from modal data [19], it can also be used to parameterise physical tyre models used in multi-body simulations, such as the FTire [20]. Typically, such models require cleat testing to identify many of their structural parameters. Cleat testing involves the tyre rolling over cleats on purposely

designed rest-rigs which constrain the vertical motion of the wheel and measure the resulting force as the cleat passes under the tyre at different speeds. Given the success of the synthesized model in predicting the vertical stiffness of the tyre [19] and provided that the size of the cleat is relatively small so as not to introduce severe non-linearities in the response, a modally parameterised tyre model should show representative cleat response. In this respect, the proposed method is more economical than cleat testing in that it does not require the use of costly test benches. On the other hand, during cleat testing, other aspects of a tyre model may be identified, such as the tread stiffness and damping, as well as corrective parameters that aim to improve the correlation between measured and simulated impact loads. The latter tend to be severely non-linear so that a mere superposition of linear radial/tangential modal responses cannot offer the required fidelity. Where high fidelity in terms of durability loads is required, cleat-test-based identification is likely to give much better results.

6. References

[1] Geng Z, Popov AA, Cole DJ. Measurement, identification and modelling of damping in pneumatic tyres. *International Journal of Mechanical Sciences* 2007; 49: 1077-1094.

[2] Popov AA, Geng Z. Modelling of vibration damping in pneumatic tyres. *Vehicle System Dynamics* 2005; 43(s1): 145-155.

[3] Chengjian F, Hui P, Dihua G. Research on tire modal testing analysis. In: *Proceedings of 2005 SEM Annual Conference & Exposition on Experimental and Applied Mechanics*, Portland, USA, 2005, pp. 689-695.

[4] Guan DH, Yam LH, Mignolet MP et al. Study of experimental modal analysis on tires. In: *Proc Int Modal Anal Conf IMAC*, Kissimmee, FL, USA, 8-11 Feb 1999, pp. 385-390.

[5] Yam LH, Guan DH, Zhang AQ. Three-dimensional mode shapes of a tire using experimental modal analysis. *Experimental Mechanics* 2000; 40(4): 369-375.

[6] Andersson P, Larsson K, Wullens F, et al. High frequency dynamic behaviour of smooth and patterned passenger car tyres. *Acta Acustica United with Acustica* 2004; 90: 445-456.

[7] Lopez I, Blom REA, Roozen NB, et al. Modelling vibrations on deformed rolling tyres – a modal approach. *Journal of Sound and Vibration* 2007; 307: 481-494.

[8] Lopez I, V Doorn RRJJ, V D Steen R, et al. Frequency loci veering due to deformation in rotating tyres. *Journal of Sound and Vibration* 2009; 324: 622-639.

[9] Guan Y, Cheng G, Zhao G, et al. Investigation of the vibration characteristics of radial tires using experimental and numerical techniques. *Journal of Reinforced Plastics and Composites* 2011; 30(24): 2035-2050.

[10] Chengjian F, Dihua G. Tire modelling for vertical properties including enveloping properties using experimental modal parameters. *Vehicle System Dynamics* 2003; 40(6): 419-433.

[11] Guan D, Fan C, Xie X. A dynamic tyre model of vertical performance rolling over cleats. *Vehicle System Dynamics* 2005; 43(s1): 209-222.

[12] Tsinias V. *A hybrid approach to tyre modelling based on modal testing and non-linear tyre-wheel motion*. PhD Thesis, Loughborough University, UK, 2015.

[13] Ewins DJ. *Modal testing*. 2nd ed. Baldock: Research Studies Press LTD, 2000

[14] Maia NMM, Silva JMM et al. *Theoretical and experimental modal analysis.* Taunton: Research Studies Press LTD, 1997.

[15] Yam LH, Guan DH, Zhang AQ. Three-dimensional mode shapes of a tire using experimental modal analysis. *Experimental Mechanics* 2000; 40(4): 369-375.

[16] Dobson BJ. A straight-line technique for extracting modal properties from frequency response data. *Mechanical Systems and Signal Processing* 1987; 1(1): 29-40.

[17] Niedbal N. Analytical determination of real normal modes from measured complex responses. In: *Proceedings of 25th Structures, Structural Dynamics and Materials Conference*, Palm Springs, CA, USA, 1994, pp. 292-295.

[18] Tsotras A, Mavros G. The simulation of in-plane tyre modal behaviour: a broad modal range comparison between analytical and discretised modelling approaches. *Vehicle System Dynamics* 2009; 47(11): 1377-1400.

[19] Tsinias V, Mavros G. Tyre modelling by combination of modal testing and non-linear tyre-wheel motion. In: 4th International Tyre Colloquium – Tyre Models for Vehicle Dynamics Analysis (ed. P. Gruber and R.S. Sharp), Surrey, UK, 20-21 April 2015, pp. 342-351.

[20] Gipser M. FTire: A physically based application-oriented tyre model for use with detailed MBS and finite-element suspension models. *Vehicle System Dynamics* 2005; 43: 76-91.